atmosphere

Article

Probability Forecasting of Short-Term Short-Duration Heavy Rainfall Combining Ingredients-Based Methodology and Fuzzy Logic Approach

Fuyou Tian [1], Xiaoling Zhang [1], Kun Xia [2,*], Jianhua Sun [3] and Yongguang Zheng [1]

[1] National Meteorological Center, China Meteorological Administration, Beijing 100081, China; tianfy@cma.gov.cn (F.T.); zhangxl@cma.gov.cn (X.Z.); zhengyg@cma.gov.cn (Y.Z.)
[2] State Key Laboratory of Numerical Modeling for Atmospheric Sciences and Geophysical Fluid Dynamics, Institute of Atmospheric Physics, Chinese Academy of Sciences, Beijing 100029, China
[3] Key Laboratory of Cloud-Precipitation Physics and Severe Storms, Institute of Atmospheric Physics, Chinese Academy of Sciences, Beijing 100029, China; sjh@mail.iap.ac.cn
* Correspondence: xiakun@lasg.iap.ac.cn

Abstract: Highly convection-related short-duration heavy rainfall (SDHR), defined as rainfall greater than 20 mm h^{-1} of a whole hour, causes severe damage every year in China. An objective forecasting method is developed to provide guidance products for the short-term probability of SDHR. Representative parameters of environmental moisture content, instability, and dynamical forcing are selected as predictors based on the ingredients-based methodology. The predictors are selected by comparing their ability to discriminate between SDHR and both no rainfall and ordinary rainfall with hourly rainfall records and the NCEP reanalysis dataset during the warm seasons of 2002 and 2009. A fuzzy logic approach is obtained for the calculation of SDHR probability. Intervals of intensities are obtained based on specific percentiles and various weight settings examined. The probabilistic SDHR forecasts during the 2015 warm seasons with the NCEP GFS dataset are obtained, and forecasts are evaluated by using an operational used spatial verification method. Results show that the reference operational SDHR forecasts are surpassed by the 00–12 h period objective SDHR forecasts measured with the maximum critical success index (CSI), and even the average CSI (CSI_{ave}) for the top groups is better than the reference. The guidance SDHR products are skillful within 60 h. Although the weights vary significantly, the short-term patterns of the SDHR probability are mainly determined by the environmental conditions. The objective forecasting method is ingredients-based but is combined with fuzzy logic algorithms. The new approach provides a feasible exploration of the convective weather phenomenon.

Keywords: short-duration heavy rainfall (SDHR); probability forecasts; ingredients-based methodology; fuzzy logic approach

Citation: Tian, F.; Zhang, X.; Xia, K.; Sun, J.; Zheng, Y. Probability Forecasting of Short-Term Short-Duration Heavy Rainfall Combining Ingredients-Based Methodology and Fuzzy Logic Approach. *Atmosphere* **2022**, *13*, 1074. https://doi.org/10.3390/atmos13071074

Academic Editor: Tomeu Rigo

Received: 6 June 2022
Accepted: 4 July 2022
Published: 7 July 2022

1. Introduction

The hourly rainfall within a whole hour greater than 20.0 mm h^{-1} is defined as a short-duration heavy rainfall (SDHR) event by the National Meteorological Center (NMC), China Meteorological Administration (CMA). SDHR occurs throughout the tropics and mid-latitude regions [1–4]. SDHR is also the leading cause of inaccurate quantitative precipitation forecasting (QPF). Extreme SDHR is often reported in extreme torrential rainfall events [5–9]. SDHR can also cause flash floods [10] and threaten aircraft safety [11]. Numerical weather prediction (NWP) models can provide high-quality QPF for lower rainfall grades, but nevertheless, many works are needed for the heavier ones due to their convective properties [12,13]. The accurate short-term forecasting of SDHR is therefore crucial if responsive measures are to be taken within an adequate timeframe.

The feasibility of operational SDHR forecasts based on environmental recognition has been documented in theoretical studies and statistical reports. SDHR can be estimated theoretically by multiplying the precipitation efficiency, the ascent rate, and the water vapor mixing ratio of the rising atmosphere of the precipitating system [14]. Nevertheless, there are challenges in obtaining values for the influencing factors. Fankhauser [15] found that the precipitation efficiency varies between events. May et al. [16] examined numerous examples of shallow, deep, and decaying convection, and reported that the large-amplitude vertical motion in deep convection is also observed in shallow convection. Lepore et al. [17] reported that the hourly rainfall intensity could be influenced by moisture availability and vertical instability. Lenderink et al. [18] documented that the most extreme hourly rainfall is accompanied by substantial large-scale upward motion and the convergence of moisture. The importance of stronger synoptic-to-mesoscale forcing for ascent and greater total column moisture content for extreme short-term precipitation has also been reported [19]. These studies show that the environmental conditions favoring high-intensity rainfall have certain features in common, such as sufficient moisture content, strong instability, and substantial upward motion, but emphasize different aspects. Although the synoptic patterns and the associated environmental conditions are similar, they are never identical. The ever-changing environmental conditions challenge the manually drawn operational SDHR forecasts.

Operational SDHR forecasts show that short-term predictions can be made by analyzing the environmental conditions of the atmosphere. The operational short-term SDHR forecasts are produced by analyzing the moisture content, the instability, and the probable dynamical lifting mechanisms using data provided by the NWP models. The process can be identified as a combination of checklists, decision trees, and experience [20]. The operational SDHR contours are produced manually and issued three times a day during the warm seasons at 06:00, 10:00, and 17:00 Beijing Time (BT = UTC + 8) [21]. The forecasts with 24-h coverage for day two and day three are treated as outlooks. The predicted areas are shaded in the issued products (available at http://www.nmc.cn/publish/bulletin/swpc.html, accessed on 1 July 2022).

Some preliminary studies have been carried out to improve the performance of the operational SDHR forecasts over China. Tian et al. [22] analyzed parameters representing the thermodynamic, moisture, and kinematic conditions of the atmosphere and found that the moisture content and instability indicators perform better if all the parameters are compared together. Divergence of 925 hPa (DIV_{925}), the best kinematic indicator, is only listed as 17th. The best vertical wind shear (SHR3 compared with SHR1 and SHR6) is only listed at 22nd. This is to some degree in conflict with the preliminary understanding that dynamic factors play important roles [19,20]. The importance of kinematic indicators is significantly undervalued if parameters are just put together for comparison. By classifying the parameters into indicators of moisture content, instability, and dynamic conditions, and dividing the hourly rainfall into no rainfall (less than 0.1 mm h^{-1}), ordinary rainfall (intensities between 0.1 and 19.9 mm h^{-1}), and SDHR (greater than 20.0 mm h^{-1}), Tian et al. [23] used millions of hourly rainfall records to study the performance of different parameters as indicators. Results show that the precipitable water (PWAT), the best lifted index (BLI), the K index (KI), and the DIV_{925} are good at simultaneously discriminating SDHR from no rainfall and ordinary rainfall. The results provide solid foundations for understanding the environmental conditions favoring SDHR. However, there are some problems to be solved for manually producing SDHR forecasts: subjective, large-scale systems are captured but there is negligence on relatively small systems, and there is not enough time to investigate the full environmental conditions.

Objective short-term convection forecasting methods have been developed but with obvious disadvantages. Li et al. [24] developed an overlapping method to predict the areas of intense convection. More than ten indices with similar representative properties are used for that method, and the area that fulfills the multi-thresholds is considered as the target area. Logistic regression models are used for intense convection prediction [25,26], but with similar problems as [24]. Most of them do not have a solid physical basis, and even worse, they do not provide SDHR forecasts. Hill et al. [27] developed a random forests method with some physical understanding to forecast severe weather, but usability for SDHR is not verified. This paper explores a new approach based on the ingredients-based methodology. The basis for the newly developed method is that adequate moisture content, some instability, and favorable dynamical forcing are required if SDHR is expected. These three components are necessary for deep, moist convection [14]. The candidate parameters are divided into different classes according to their properties. The predictors are selected by comparing the significance of distinguishing ordinary rainfall and no rainfall within the class it belongs to. A piecewise linearization method is used for the selected predictors to indicate the intensities. A fuzzy logic method is adopted to display the multiple combination modes, in other words, the probability distribution of SDHR under multiple environmental conditions.

The paper is organized as follows. Section 2 describes the data used, the selection of predictors, the construction of the method, and the evaluation method. The evaluation results are given in Section 3. Section 4 illustrates an application of the objective method to two case studies under different synoptic patterns, and a summary and discussion are given in Section 5.

2. Data and Methods

2.1. Data Source

We use quality-controlled hourly rainfall data of 411 climate observation stations (Figure 1a) from CMA, and the NCEP reanalysis dataset (https://rda.ucar.edu/datasets/, accessed on 22 April 2022) from May to September (warm seasons) during 2002 and 2009 to select predictors. The climate observation stations are widely distributed in central-eastern China (Figure 1a). The stations can only record liquid precipitation. Thus, the span of available data varies significantly. Rain can be reported in January in south China, while no records are available even at the end of April in northeast China. Only the observations between 1 May and 30 September are used in this study for the broad applicability of the forecasting method. The NCEP GFS dataset for the 2015 warm season is adopted to produce the forecasts of SDHR. Data for the SDHR reported by automatic weather stations (AWS) are also used for verification (Figure 1b).

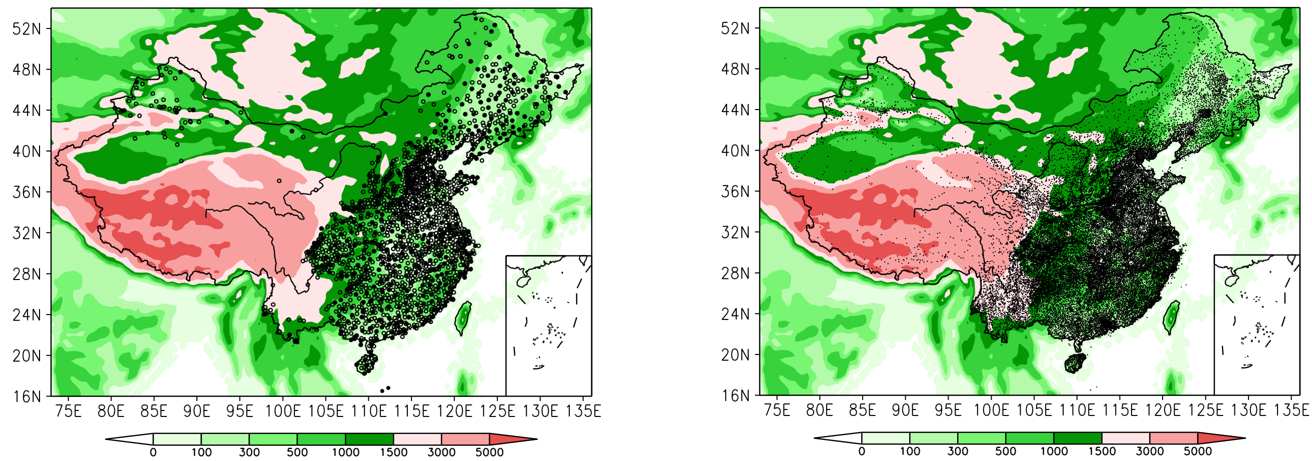

(**a**) (**b**)

Figure 1. Distribution of (**a**) climate observation (solid points) and verification (circles) stations and (**b**) automatic weather stations (AWS).

The NCEP reanalysis dataset has a spatial resolution of $1^{\circ} \times 1^{\circ}$ and a temporal resolution of four times a day at 02:00, 08:00, 14:00, and 20:00 BT [28]. Table 1 lists the parameters which are possibly useful to represent the favorable environmental conditions of SDHR, including moisture content, instability, and dynamical forcing. The instability parameters include the BLI, the best convective available potential energy (BCAPE), etc. The PWAT, specific humidity, relative humidity, and water vapor flux divergence are treated as candidate indicators of the moisture content, whereas the dynamical forcing and vertical wind shear are considered to be kinematic indicators.

Table 1. Description of referred parameters used to indicate the environmental moisture content, instability, and lifting conditions. S1 and S2 represent the overlapping sizes of the relative frequencies between SDHR and ordinary rainfall (S1), and SDHR and no rainfall (S2). S is the multiplication of S1 and S2. The bolded are the minimum values within its group. The parameters selected as predictors are signed with *.

Classification	Abbr.	Indices	Unit	S1	S2	S
Moisture	PWAT *	Total precipitable water	mm	**0.70**	0.41	**0.287**
	Q_{925}	Specific humidity of 925 hPa	g kg^{-1}	**0.70**	0.49	0.343
	RH_{850}	Relative humidity of 850 hPa	%	0.75	0.42	0.315
	Q_{850}	Specific humidity of 850 hPa	g kg^{-1}	0.76	0.44	0.334
	RH_{700}	Relative humidity of 700 hPa	%	0.77	0.41	0.316
	Q_{700}	Specific humidity of 700 hPa	g kg^{-1}	0.78	**0.40**	0.312
	DVF_{700}	Water vapor flux divergence of 925 hPa	g s^{-1} cm^{-2} hPa^{-1}	0.80	0.65	0.520
	DVF_{850}	Water vapor flux divergence of 850 hPa	g s^{-1} cm^{-2} hPa^{-1}	0.90	0.78	0.702
	DVF_{925}	Water vapor flux divergence of 700 hPa	g s^{-1} cm^{-2} hPa^{-1}	0.98	0.97	0.951
Instability	BLI *	Best lifted index	°C	**0.52**	0.47	**0.244**
	$\theta_{se}925$	925 hPa potential pseudo-equivalent temperature	K	0.63	0.51	0.321
	$\theta_{se}850$	850 hPa potential pseudo-equivalent temperature	K	0.64	0.45	0.288
	BCAPE	Best convective available potential energy	J kg-1	0.67	0.73	0.489

Table 1. *Cont.*

Classification	Abbr.	Indices	Unit	S1	S2	S
	T_{850}	850 hPa Temperature	°C	0.68	0.66	0.449
	KI*	K index	°C	0.70	**0.37**	**0.259**
	DT85	Temperature difference of 850 hPa and 500 hPa	°C	0.92	0.90	0.828
	TT	Total totals	°C	0.96	0.83	0.797
Lifting	SHR6	0–6 km vertical wind shear	m s^{-1}	**0.81**	0.92	0.745
	DIV_{925} *	925 hPa divergence	s^{-1}	0.83	**0.64**	**0.531**
	SHR3	0–3 km vertical wind shear	m s^{-1}	0.88	0.71	0.625
	DIV_{850}	850 hPa divergence	s^{-1}	0.92	0.90	0.828
	SHR1	0–1 km vertical wind shear	m s^{-1}	0.97	0.98	0.951

2.2. Climatology of SDHR

SDHR mainly occurred during the warm seasons. For the consistent period over different areas of China, the SDHR between 1 May and 30 September is used. Here, we mainly analyze the monthly variation to provide a reference for the determination of studied months. The eight-year hourly rainfall data show that the monthly SDHR usually peaked in June, July, or August (Figure 2). The monthly number of SDHR in May is generally between 200 and 300. The average number is about 250. In June, the number of SDHR increased to about 400. There are approximately 500 SDHR in July. In August, the number of SDHR shows a slight decrease compared with July, before decreasing sharply to about 200 in September. This variation is similar to that reported in previous studies [4,29] and is in good agreement with the yearly variation in torrential rainfall [30].

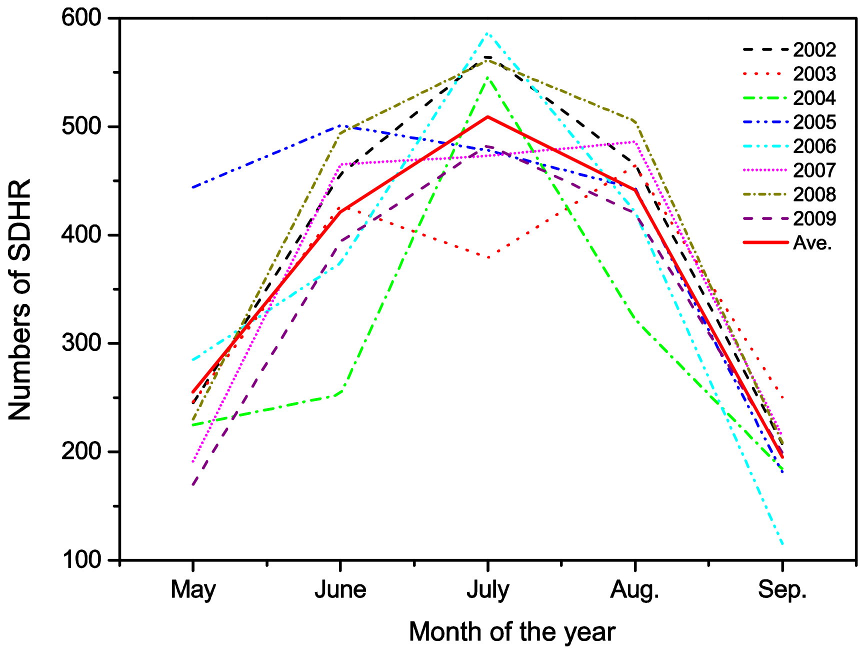

Figure 2. Monthly variation of the number of SDHR during the warm seasons of eight years. The bold solid red line represents the variation of the monthly average SDHR.

2.3. Selection of Predictors

The climate observation stations are mainly located in central and eastern China (Figure 1a). There are 24 records for every station in one day, while there are only four time moments for the NCEP reanalysis data. A temporal matching process is executed to use the information provided by both observations and the NCEP reanalysis data. The 24 hourly rainfall records in a day are divided into four groups with the four times of 02:00, 08:00, 14:00, and 20:00 BT of the NCEP reanalysis dataset in the center. The maximum hourly rainfall in each group is selected. Using this process, the size of the SDHR sample is about 11,400, whereas the sizes of the no rainfall and ordinary rainfall samples are about 350,000 and 1,500,000, respectively. The values of the parameters in Table 1 at the climate observation stations are obtained by bilinear interpolation from the grid points of the NCEP reanalysis data. The characteristics of the parameters for SDHR, no rainfall, and ordinary rainfall are then obtained.

We select only the most representative parameters within each group of moisture content, instability, and dynamic lifting as predictors. The selection of predictors is based on the common understanding that certain moisture content, some instability, and favorable dynamical forcing are the required environmental components for SDHR. The overlapping size of the relative frequencies of SDHR and ordinary rainfall (S1) and SDHR and no rainfall (S2) are calculated for all parameters (Table 1). The overlapping size provides an objective measure for the selection of predictors. A smaller overlapping size represented by S1 or S2 indicates better discrimination between SDHR and no rain, and ordinary rainfall and SDHR, respectively. The multiplication S of S1 and S2 as an overall index for each parameter is also obtained. A smaller S indicates better overall discrimination.

The overlapping size shows that S1 for both PWAT and specific humidity of 925 hPa (Q_{925}) equals 0.70. However, the S2 for PWAT is 0.41, whereas the value for Q_{925} is 0.49. The S for PWAT is 0.287, while the others are greater than 0.310. The S shows that PWAT has the overall best performance compared with the other moisture indicators. For the instability indicators, the S1 for the BLI is 0.52, the smallest value. KI has a smaller S2. S shows that BLI is the best overall indicator. However, the difference between BLI and KI is much smaller. Both the BLI and KI are selected as instability indicators. For dynamic forcing, S1 values for SHR6 and DIV_{925} are similar, but S2 for DIV_{925} is much smaller than that for SHR6. S shows that DIV_{925} performs best among the verified dynamic indicators. PWAT, BLI, KI, and DIV_{925} are therefore selected as predictors. Figure 3 shows the distributions of the relative frequencies of the selected predictors. It should be noted that DIV_{925} could not represent the correct dynamic conditions of higher latitude areas.

Box-and-whisker plots of different hourly rainfall intensities provide clear images of the overlapping portion, whereas the overlapping sizes of the relative frequencies provide objective measures (Figure 3). Figure 3a shows that more than 99% of SDHR occurs in environments with PWAT greater than 28 mm. The median PWAT for SDHR is 58 mm. Only about 25% of ordinary rainfall events occur with PWAT greater than 58 mm, and the percentage for no rainfall is much less than 25%. Both the BLI and KI are selected as good indicators of instability. More than 80% of SDHR occurs when the BLI is less than -0.6 °C (Figure 3b). More than 80% of the SDHR has a KI greater than 35.45 °C (Figure 3c), but the percentage for ordinary rainfall is less than 50%, and for no rainfall it is much less than 25%. The DIV_{925} shows that more than 80% of SDHR occurs under a negative DIV_{925} environment (Figure 3d). It is a favorable dynamical forcing condition.

The selected predictors are physically meaningful. Trenberth [31] shows that a large part of the moisture had already been in the air as storms formed over areas outside the tropics. The BLI indicates latent instability [32]. The KI has three components: the temperature difference between 850 and 500 hPa, the 850 hPa dew point temperature, and the difference between the 700 hPa temperature and the dew point temperature. The temperature difference between 850 and 500 hPa itself is usually used as an instability indicator. The 850 hPa dew point temperature is also used to indicate the absolute moisture content at low levels. The difference between the 700 hPa temperature and the dew point temperature is usually used to indicate saturation. Thus, KI represents both instability and the moisture content, making KI a good discriminator of SDHR from no and ordinary rainfall. DIV_{925} is often used to characterize near-surface dynamic conditions.

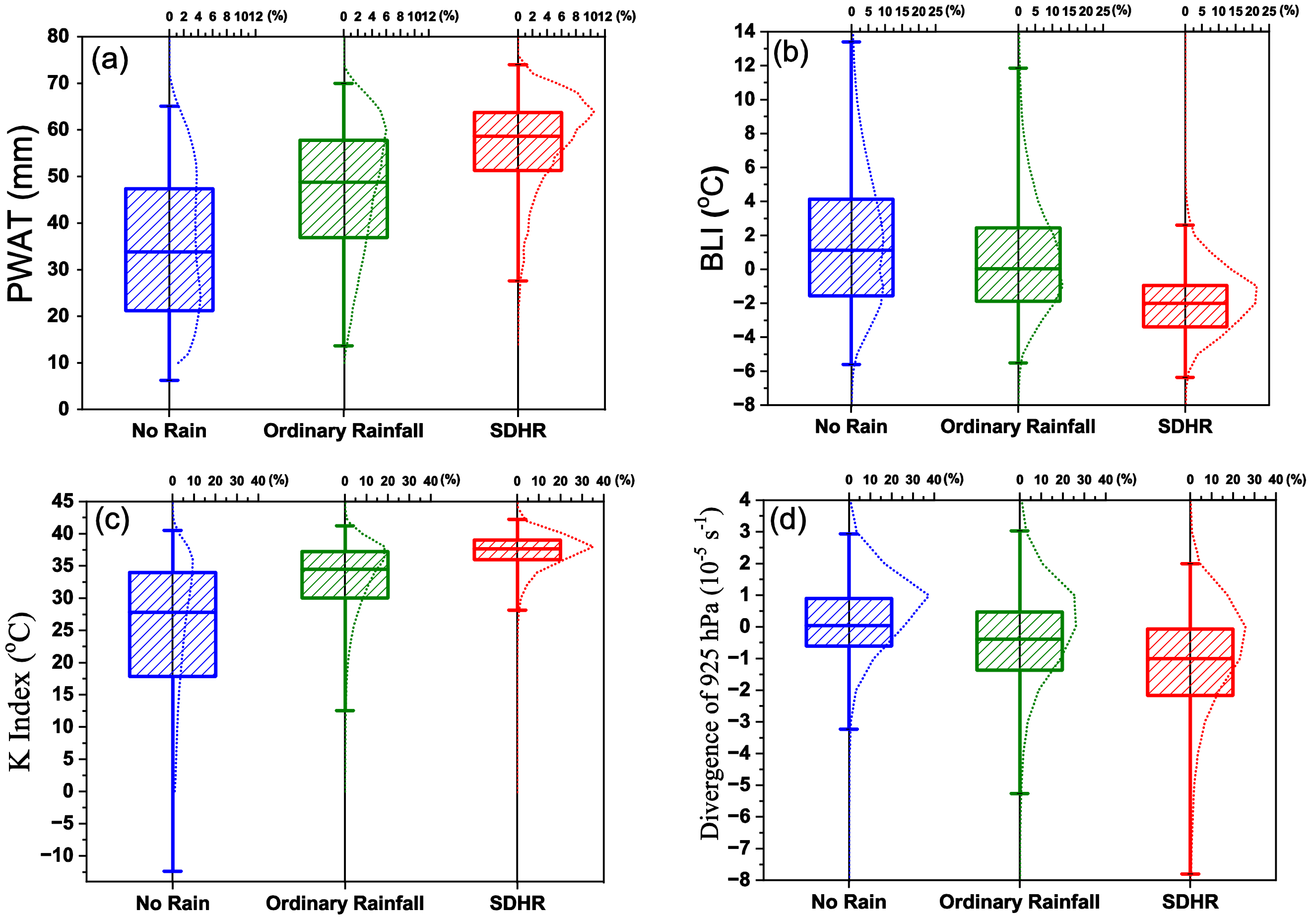

Figure 3. The box-and-whisker plots of (**a**) PWAT, (**b**) BLI, (**c**) KI, and (**d**) DIV_{925} for no rainfall, ordinary rainfall, and SDHR. The three lines of the boxes indicate the 25th, 50th, and 75th percentiles. The upper and lower short bars indicate the 1st and 99th percentiles, respectively. The dashed lines with calibrations at the upper level show the distribution of the corresponding relative frequencies of the samples.

For the selected predictors, the correlation coefficients for SDHR are also calculated. All the correlation coefficients are significant at the 0.05 significant levels with the two-tailed test of significance. The highest correlation coefficient is 0.5406 and is given by PWAT and KI; the absolute values of the other correlation coefficients are all less than 0.35. The correlation coefficients indicate that the selected predictors are not strongly correlated and are representative of the environmental conditions characterized.

2.4. Fuzzy Logic Algorithm for the Probability of SDHR

The distribution of relative frequencies of the three-hourly rainfall intensities for a specific predictor shows that the recognition of SDHR from both ordinary rainfall and no rainfall conforms to the fuzzy set theory. Fuzzy logic is an extension of set-theoretic multivalued logic [33] that can deal with problems relating to ambiguous and imprecise judgments. Fuzzy logic algorithms have been used in the nowcasting of convection, the prediction of lightning and afternoon thunderstorms, and the identification of radar echoes [34–37]. However, there is no report of the application of the fuzzy logic algorithm to the prediction of short-term SDHR. By adopting the fuzzy logic algorithm, the probability of SDHR (Ps) with selected predictors can be derived as:

$$P_s = \frac{\sum_{i=1}^{i=n} f_i w_i}{\sum_{i=1}^{i=n} w_i} \quad (1)$$

where n is the number of predictors (n = 4 in this study), w_i is the corresponding weight of the ith parameter, and f_i is the membership function of the ith parameter.

There are several ways to obtain the membership functions [35–37]. We adopted the membership functions using a piecewise linearization method by dividing the selected predictors into five grades based on the 20th, 40th, 60th, and 80th percentiles (Figure 4). A piecewise linearization method is a way to approximate a nonlinear objective function by adding extra binary variables, continuous variables, and constraints [37]. The piecewise linearization method is used arbitrarily due to the difficulty in defining proper membership functions to distinguish SDHR from ordinary rainfall and no rainfall simultaneously. With the piecewise linearization method, the five membership function grades 0.2, 0.4, 0.6, 0.8, and 1.0 are arbitrarily fixed (Figure 4). The relative strength could be represented with this piecewise linearization method. Taking PWAT and BLI as examples, a higher PWAT means an environmental condition with more moisture content, while a smaller BLI indicates a more unstable atmospheric environment. Statistics show that there are some thresholds if SDHR is expected. The fuzzy logic algorithm is applied only if these thresholds are met. Table 2 shows that the thresholds should be fulfilled to reduce the number of false alarms. The precipitation provided by the NCEP GFS is also used as a threshold (Table 2). Most thresholds are obtained by calculating the fifth percentile (the 95th percentile for the BLI and DIV_{925}).

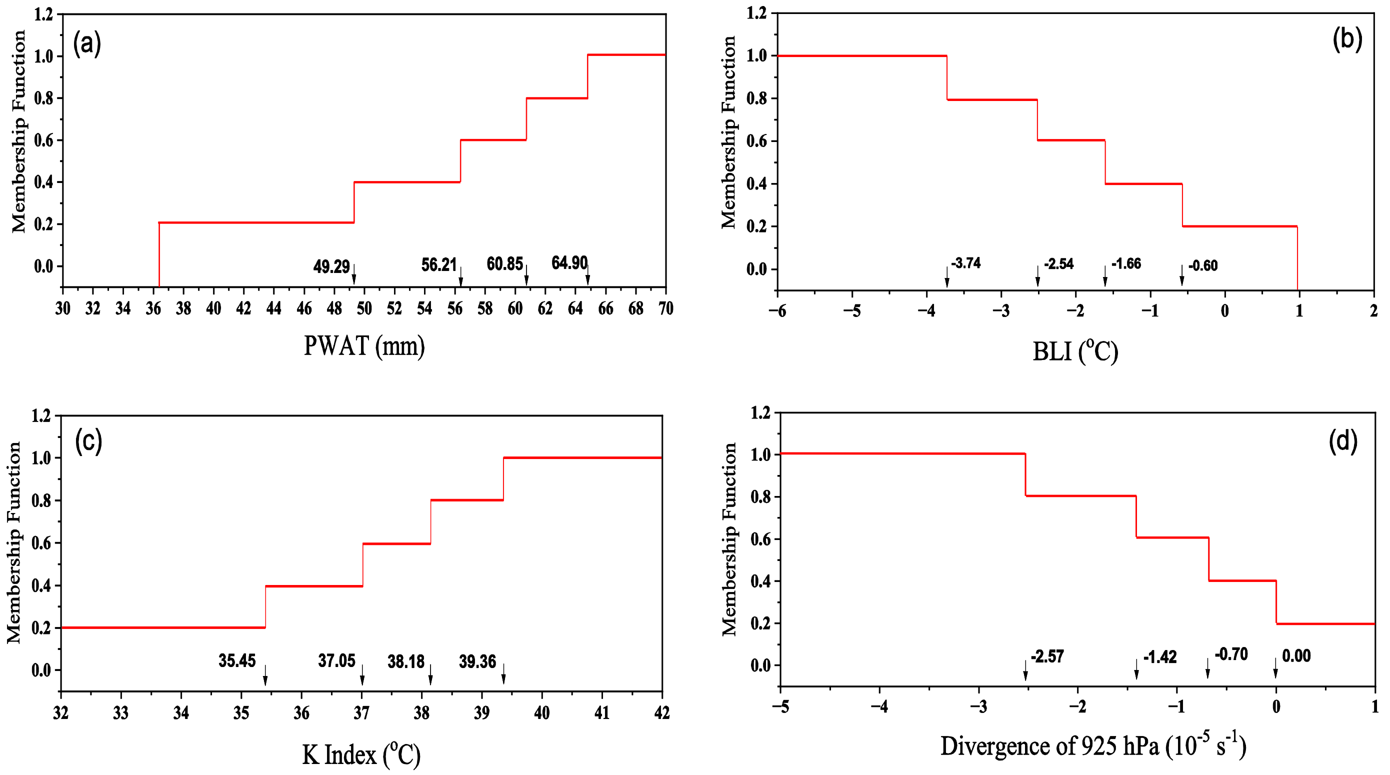

Figure 4. Membership functions of (**a**) PWAT, (**b**) BLI, (**c**) KI, and (**d**) DIV_{925}. The values and arrows indicate the thresholds used for the grade division of the membership functions.

Table 2. Thresholds of parameters used to define SDHR.

Abbrev.	PWAT	RH_{850}	BLI	KI	DIV_{925}	T_{850}	TP
Unit	mm	%	°C	°C	s^{-1}	°C	mm
Threshold	≥30	≥70	≤0.96	≥32.0	$\leq 1.0 \times 10^{-5}$	≥15	≥1.0

The determination of weights is also important. By setting a weighted step of 0.1, 84 groups of feasible weight settings are executed. No zero weight is allowed to follow, on the basis that moisture content, instability, and lifting force are all necessary for SDHR, although the BLI and KI are both considered to be instability indicators. Another specific group with an assigned equal weight of 0.25 is also examined for comparison.

With the results mentioned above, the fuzzy logic algorithm is executed grid by grid. The procedure is as follows:

Step 1: The obtaining of the physical quantity fields of the predictors provided by NWP models at a given forecast moment.

Step 2: The check of thresholds according to Table 2. Grids values that do not meet the thresholds given in Table 2 are judged as not favoring SDHR.

Step 3: The obtaining of fuzzy sets according to Figure 4. The physical quantity fields of the predictors are transformed into fuzzy sets between 0.0 and 1.0. It is a normalization process of predictors.

Step 4: The obtaining of the weights. There are up to 85 weight groups estimated in this study.

Step 5: The obtaining of the SDHR probability according to Equation (1).

SDHR probability field at a given forecast moment is obtained by executing steps from 1 to 5.

2.5. Evaluation Method

Prediction within 96 h with three-hour intervals between 1 April and 30 September, provided by NCEP GFS 1° × 1°dataset, a coverage of later spring, a whole summer, and the early autumn, in 2015, initialized at 08:00 BT, is obtained. For ease of comparison with the operational SDHR forecasts, the 12-hour interval SDHR forecasts are obtained by comparing the five three-hour interval forecasts. The highest probability is considered to be the 12-hour SDHR probability for every grid.

A spatial verification method is adopted that considers the dependence of extreme convective rainfall on the gauge network density. Schroeer et al. [38] shows that operational gauge networks underrate extreme convective rainfall falling over small areas. With the spatial verification method, the AWS observations within 40 km of verification stations are searched [21,22]. The hourly rainfall reported by the 1827 verification stations (Figure 1a) and the AWS (Figure 1b) is used during the verification period. If both the verification stations and the AWS within 40 km report no SDHR, it is considered as no SDHR; otherwise, SDHR is confirmed. This approach will, to some extent, compensate for a failed detection as a result of the spatial scale of local SDHR. The bilinear interpolation method is adopted to obtain the forecast results of the verification stations.

Using the preprocessed SDHR observations and predictions, the performance of the probabilistic SDHR forecast is evaluated with thresholds at 2.5% increments to create a contingency table. Taking 2.5% as an example, the stations with a probability greater than 2.5% are considered as yes forecasts. Otherwise, they are considered as no forecasts. Then, hits, false alarms, misses, and correct rejections denoted by H, FA, M, and CR (Table 3) are calculated. For the operational SDHR forecasts, the verification stations located within the predicted areas are taken as yes forecasts. Otherwise, no forecasts are confirmed. Skill scores are then computed for the objective and operational SDHR forecasts. Metrics including the critical success index (CSI), the bias, the probability of detection (POD), and the false alarm rate (F) are used. The calculations are as follows:

$$\mathrm{CSI} = \mathrm{H}/(\mathrm{H} + \mathrm{FA} + \mathrm{M}) \tag{2}$$

$$\text{Bias} = (\text{H} + \text{FA})/(\text{H} + \text{M}) \tag{3}$$

$$\text{POD} = \text{H}/(\text{H} + \text{M}) \tag{4}$$

$$\text{F} = \text{FA}/(\text{FA} + \text{CR}) \tag{5}$$

Table 3. The 2 × 2 contingency table for yes/no categorical verification.

		Observation	
		Yes	**No**
Forecast	Yes	H (hit)	FA (false alarm)
	No	M (miss)	CR (correct rejection)

3. Evaluation of Results

3.1. Evaluation for 00–12 h Forecasts

The 00–12 h forecasts show skillful performance compared with the operational SDHR forecast measured with the maximum CSI. The maximum CSI for all 85 groups varies between 0.31 and 0.32, around a probability of 20% (Figure 5a). The reference CSI is 0.24, the maximum value for the operational SDHR forecasts issued at different times [18]. However, the corresponding bias of the maximum CSI for each group is about 1.5, indicating an overestimate (Figure 5b). All the groups have unbiased results around the probability of about 40%. The CSI around this probability is about 0.28, a higher score than the reference. The bias for each group of weight settings decreases as the probability increases. However, the trends for the CSI of different groups are different (Figure 5a). The groups with higher maximum CSI values do not always surpass the others as the probability increases. Thus, the average CSI (CSI_{ave}) values for all 85 groups are calculated to understand the general performance of each group. The CSI_{ave} for each group is calculated by dividing the sum CSIs of every group at continuous probability points, as shown in Figure 6, by the total number of probability points. The five top groups with the highest maximum CSI and highest CSI_{ave} are colored in red and blue, respectively (Figure 5). The five top groups with the highest maximum CSI have a higher bias than the five groups with the highest CSI_{ave} at almost every probability.

Table 4. Weights of groups with the maximum CSI and CSI_{ave} for the 00–12 h forecast. No. 1–5 are listed with maximum CSI, while NO. 6–10 are listed with maximum CSI_{ave}. No. 11 in the group is assigned with equal weights. The Bias, POD, and FAR that correspond to the CSI are also given. The maximum CSI and CSI_{ave} are bolded. The maximum weight values of each group are also bolded.

No.	Weights				Skill Scores				
	PWAT	**BLI**	**DIV_{925}**	**KI**	**CSI**	**CSI_{ave}**	**Bias**	**POD**	**FAR**
1	0.1	**0.7**	0.1	0.1	**0.3202**	0.2426	1.376	0.576	0.1234
2	0.2	**0.6**	0.1	0.1	0.3201	0.2357	1.416	0.586	0.1281
3	0.1	**0.6**	0.1	0.2	0.3199	0.2377	1.413	0.585	0.1278
4	0.1	**0.5**	0.1	0.3	0.3197	0.2333	1.339	0.567	0.1190
5	0.2	**0.5**	0.1	0.2	0.3197	0.2310	1.398	0.581	0.1261
6	0.1	0.1	**0.7**	0.1	0.3120	**0.2501**	1.477	0.589	0.1370
7	0.1	0.2	**0.6**	0.1	0.3130	0.2482	1.476	0.590	0.1367
8	0.1	0.3	**0.5**	0.1	0.3144	0.2465	1.475	0.592	0.1363
9	0.1	**0.4**	**0.4**	0.1	0.3157	0.2450	1.471	0.593	0.1355
10	0.1	0.1	**0.6**	0.2	0.3126	0.2443	1.456	0.585	0.1344
11	0.25	0.25	0.25	0.25	0.3165	0.2273	1.457	0.591	0.1269

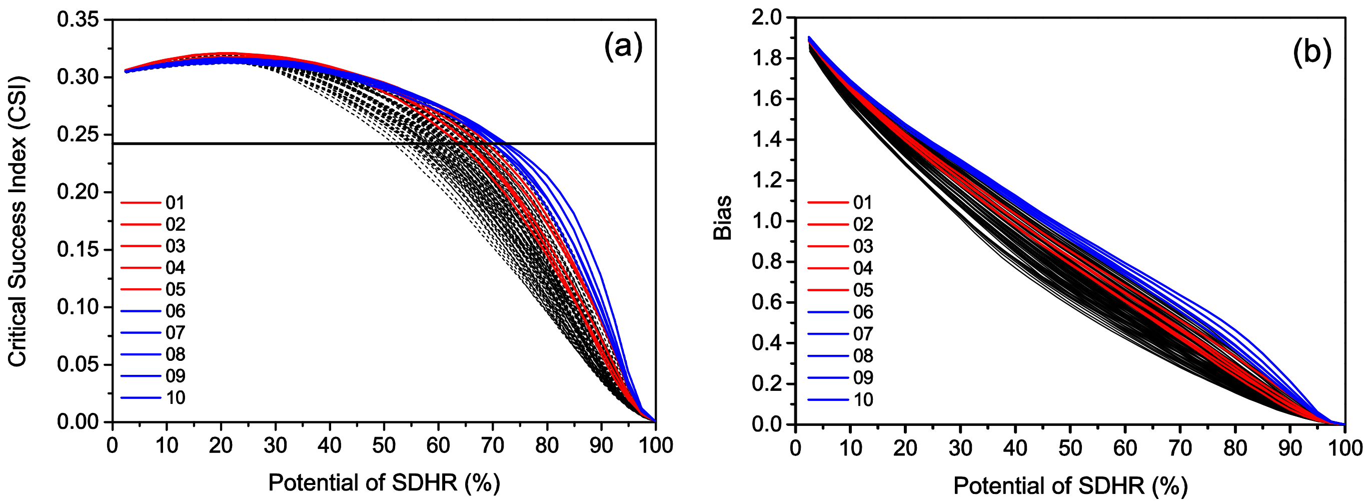

Figure 5. Variation of (**a**) CSI and (**b**) bias for the 00–12 h probability of SDHR with different weight settings. The 12-hour operational SDHR forecasts issued at 08:00 BT (horizontal black line in Figure 5a) during the 2015 warm season are shown for reference. The five red lines are the top groups with the highest maximum CSI, and the blue lines represent the top five groups with the highest maximum CSI_{ave}. The weights of the ten groups are listed in Table 4.

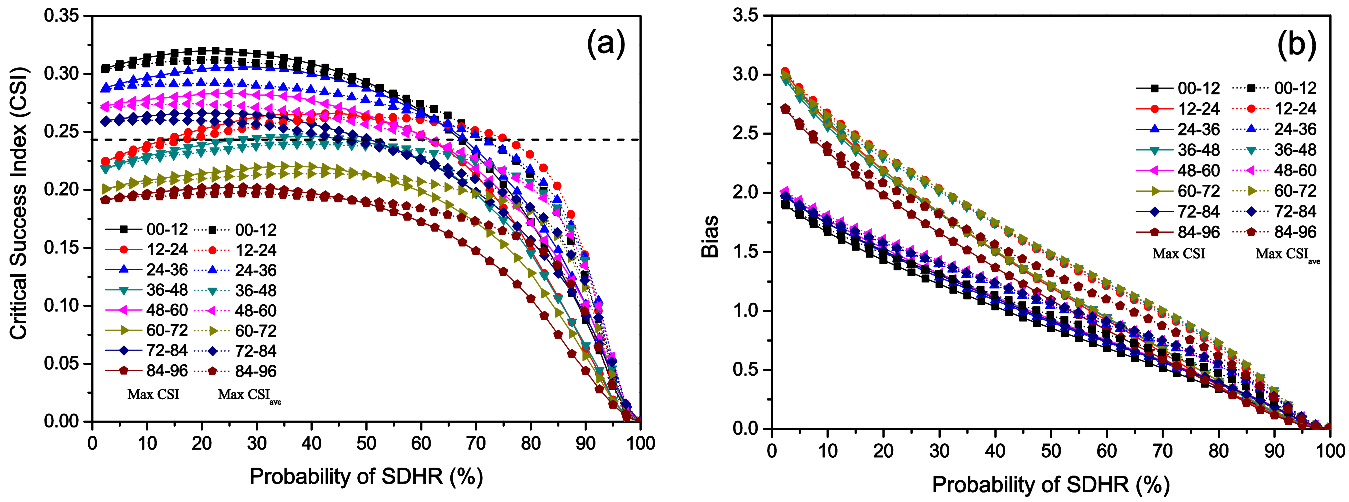

Figure 6. Variation of (**a**) CSI and (**b**) bias for 00–12, 12–24 ... 72–84, and 84–96 h probabilities of SDHR for the groups with the highest maximum CSI and the highest CSI_{ave} during the 00–12 h forecasts. The dashed horizontal line in Figure 6a represents the reference CSI.

The weights can be divided into two groups according to the proportional distribution (Table 4). The weights of the BLI and DIV_{925} play important roles for the groups with the highest maximum CSI and CSI_{ave}, respectively. For the five groups in which the weights of the BLI are much higher than the others (Table 4), the DIV_{925} weights are 0.1. The portion of instability is increased for better SDHR results. The maximum CSI for the top five groups with the highest maximum CSI is about 0.320, and the corresponding bias is about 1.4. The POD is about 0.580, and the FAR is less than 0.130, indicating skillful results. Different results are obtained for the groups with the highest CSI_{ave}. The maximum CSI_{ave} is 0.250 (No. 6 in Table 4), better than the reference. DIV_{925} has higher weights for the five groups with the highest CSI_{ave}. The difference in the weights for instability and dynamical forcing leads to different performances of the highest maximum CSI and highest CSI_{ave}. Table 4 also gives the group assigned equal weights, although this is not included in the top 10. It should be noted that even with the assigned equal weights, the maximum CSI and corresponding index are much the same as the others. The importance of different weights is not as important as previously thought.

3.2. Evaluation of Longer Period Forecasts

The longer period forecasts for the weights of the highest maximum CSI and highest CSI_{ave} during the 00–12 h forecasts are evaluated. The maximum CSI for the forecasts covering the daytime (e.g., 00–12, 24–36, 48–60, and 72–84 h) is higher than the reference CSI (Figure 6a). The maximum CSI for the nighttime forecasts (e.g., 12–24, 36–48, 60–72, and 84–96 h) is different. The maximum CSI of both groups for the 12–24 h forecasts is better than the reference. The maximum CSI for the 36–48 h forecast is almost the same as the reference. However, the maximum CSI for both groups' 60–72 and 84–96 h forecasts is smaller than the reference. The bias indicates the dependence of performance on daytime and nighttime (Figure 6b). The biases in the nighttime forecasts are higher than those in the daytime forecasts for the same probability. The diurnal variation of SDHR could cause the difference between daytime and nighttime on verification. SDHR over eastern China mainly occurs during the daytime [4,29,39].

The afternoon peak of SDHR is caused by the local thermal forcing [7,40]. The maximum atmospheric instability in the afternoon that originated from solar heating is the immediate cause [40]. The afternoon maximum atmospheric instability has been frequently observed. The NCEP reanalysis data are only four times a day at 02:00, 08:00, 14:00, and 20:00 BT. The peak of SDHR is around 18:00 BT [39], just the middle of 14:00 and 20:00 BT. The diurnal variation of detailed characteristics could not be fully revealed by the NCEP reanalysis data as the daily cycle of precipitation shows [41,42]. However, the reference value is surpassed by both weight groups within 60 h though the diurnal variation of the SDHR.

4. Performance for Oceanic and Continental Events

The performance of the two events that occurred under oceanic and continental environmental conditions is assessed. The first event was the typhoon Soudelor, which occurred on 8 August 2015. Accurate forecasting of convective precipitation produced by typhoons is still a great challenge [43]. The second event, which occurred on 15 May 2015 over southern China, is a typical spring event caused by a low-level convergence line combined with a mid-level short trough. Accurate forecasting of heavy rainfall that happens under similar synoptic patterns is still challenging due to intense convection. The selected cases represent two SDHR regimes: oceanic and continental [44]. The different environmental conditions for SDHR show the applicability of the new method.

The NCEP GFS data are also used to obtain the SDHR probabilities and environmental conditions. The spatial resolution is $1^\circ \times 1^\circ$. SDHR observations reported by all available weather stations are displayed.

4.1. The Typhoon Soudelor on 8 August 2015

The synoptic pattern had been effectively predicted several days in advance. Here, we focus mainly on the 24-h SDHR forecasts valid at 20:00 BT on 8 August 2015. The predicted 850 hPa wind field (Figure 7a) shows that the maximum westward wind was greater than 40 m s^{-1}. A large area had a negative DIV_{925}, indicating favorable low-level forcing conditions. The minimum DIV_{925} was less than -10×10^{-5} s^{-1} north of the center of Soudelor (Figure 7a). A relatively large area of DIV_{925} can be characterized as moderate to strong and strong. For the area with a negative DIV_{925}, the PWAT was greater than 49 mm, and the maximum PWAT was greater than 70 mm (Figure 7b), with the center located over the seas. The PWAT can also be characterized as moderate to strong and strong grades. The KI delivers similar information to the DIV_{925} and PWAT (Figure 7c). However, the BLI is between -2.5 and 1 °C in the main body of Soudelor (Figure 7b), which can be ranked only as moderate and weak to moderate. The environment provided at this time can be characterized by strong dynamical forcing, strong PWAT, and weak to moderate instability.

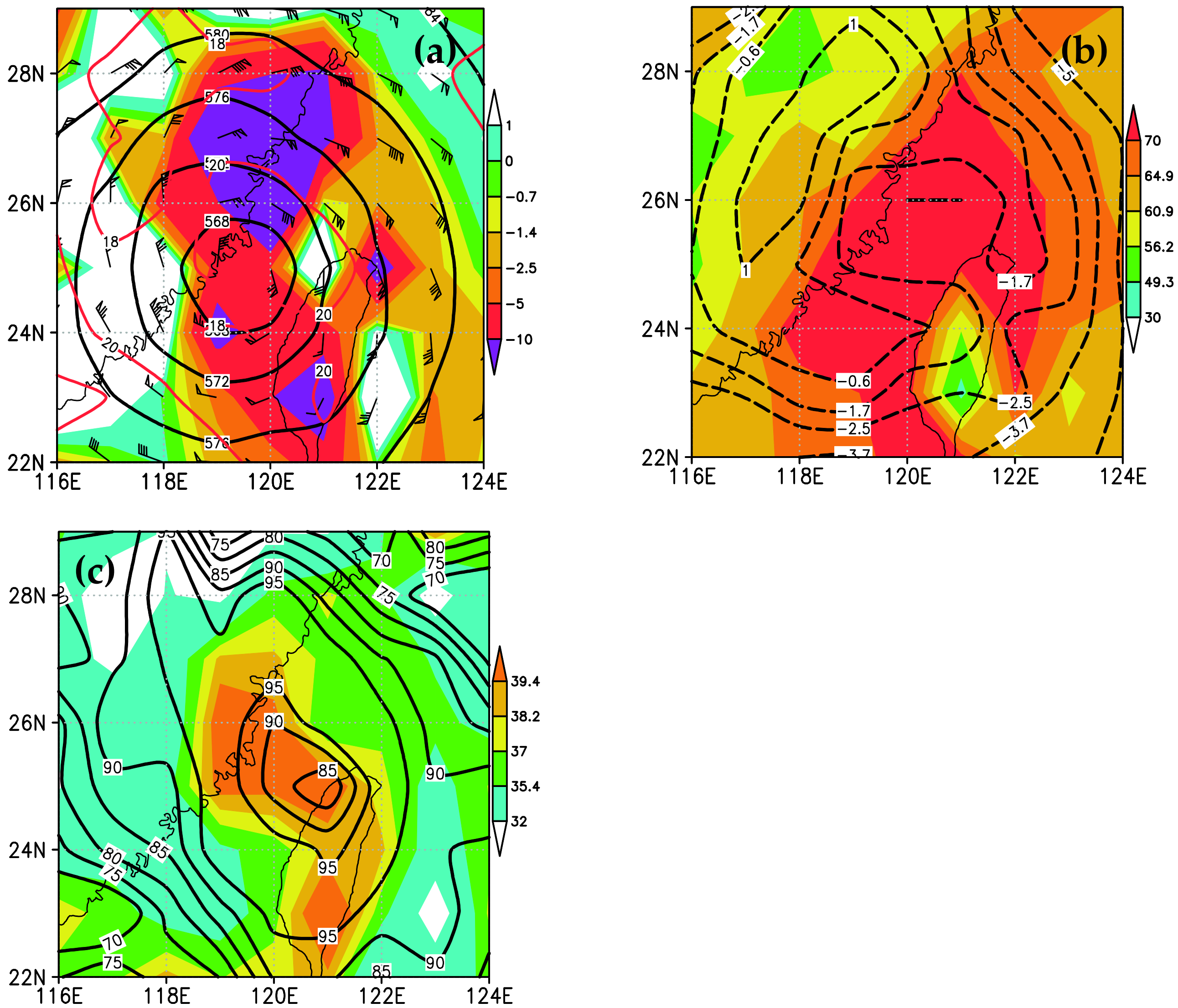

Figure 7. The 24-h synoptic pattern and parameter distribution valid at 20:00 BT on 8 August 2015 predicted by the NCEP GFS; (**a**) 925 hPa divergence (10^{-5} s^{-1}, negative shading with legend at right), 850 hPa wind field (where a half-bar represents 2 m s^{-1}, a full bar represents 4 m s^{-1}, and a flag represents 20 m s^{-1}), temperature (red line, °C), and 500 hPa isobars (solid black line). (**b**) The PWAT (shaded with legend at right) and BLI (dashed black lines, °C). (**c**) The KI (shaded with legend at right) with the 850 hPa relative humidity greater than 70% (black solid line, %). The thresholds used for the key parameters are the same or close to that given in Figure 4.

Under the predicted environmental conditions, the area with high probabilities of SDHR is mainly located in the north of Soudelor, in the southeastern coastal area of China (Figure 8). Most of the SDHR reported by AWS is predicted well. There should be much SDHR that occurred over the seas but no records are available. Figure 8a,b show the SDHR forecasts for the weights of maximum CSI and the maximum CSI$_{ave}$. As a comparison, the averaged SDHR probability and the corresponding standard deviation of the 84 groups are also given (Figure 8c,d). For this case, the maximum CSI$_{ave}$ weight group performs better than the maximum CSI weight group. Even the averaged SDHR probability shows good performance. Still, there are some misses and false alarms. The standard deviation is much smaller over the predicted field, indicating a relatively small variance between different weight settings. It is reasonable because the predicted large-scale environmental conditions are determined for a fixed time.

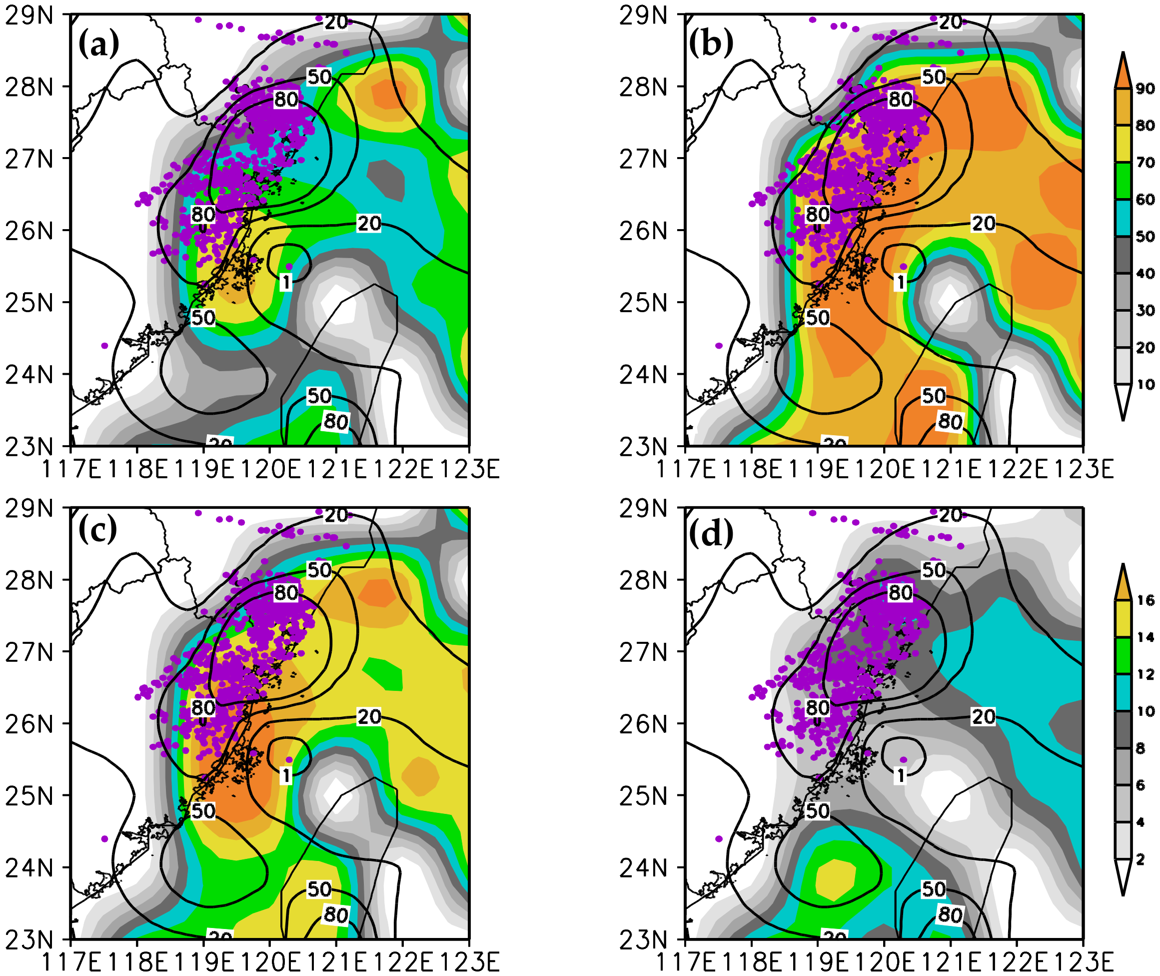

Figure 8. Comparison of the predicted 24-h SDHR probability (shaded) valid at 20:00 BT on 8 August 2015; (**a**) is for the maximum SCI group with weights of No. 1 in Table 4, (**b**) is for the maximum SCI_{ave} group with weights of No. 6 in Table 4, (**c**) is the average of the 84 groups, and (**d**) is the corresponding standard deviation of (**c**). The available SDHR observations reported by AWS from 17:00 to 23:00 BT on 8 August 2015 are shown as purple dots. The solid lines in each panel are the NCEP-GFS-predicted six-hour rainfall accumulation (mm) from 17:00 to 23:00 BT on 8 August 2015.

4.2. The Spring Event over Southern China on 15 May 2015

The 15 May 2015 example is a typical spring SDHR event. The 48-h prediction of the synoptic pattern shows that a cold low is located in northeast China. The cold air to the south of the cold low encounters warm, moist air as it moves into southern China, and a shear line is formed at lower levels (Figure 9a). The DIV_{925} along the shear line is between 1×10^{-5} and -5.0×10^{-5} s^{-1}, measured as favorable dynamical forcing conditions (Figure 4a). The moisture content measured by PWAT is greater than 50 mm over a large area, with a maximum PWAT of about 60 mm (Figure 9b). The PWAT can only be measured as moderate. A large area over the north is unfavorable for SDHR as the moisture content indicated by PWAT is lower than required. The instability indicated by the BLI shows moderate to strong and strong unstable atmospheric conditions (Figure 9b). The instability over a large area can also be classified as moderate to strong and strong, even measured by KI (Figure 9c). The environmental conditions can be recognized as strong dynamical lifting, strong instability, and only moderate moisture content.

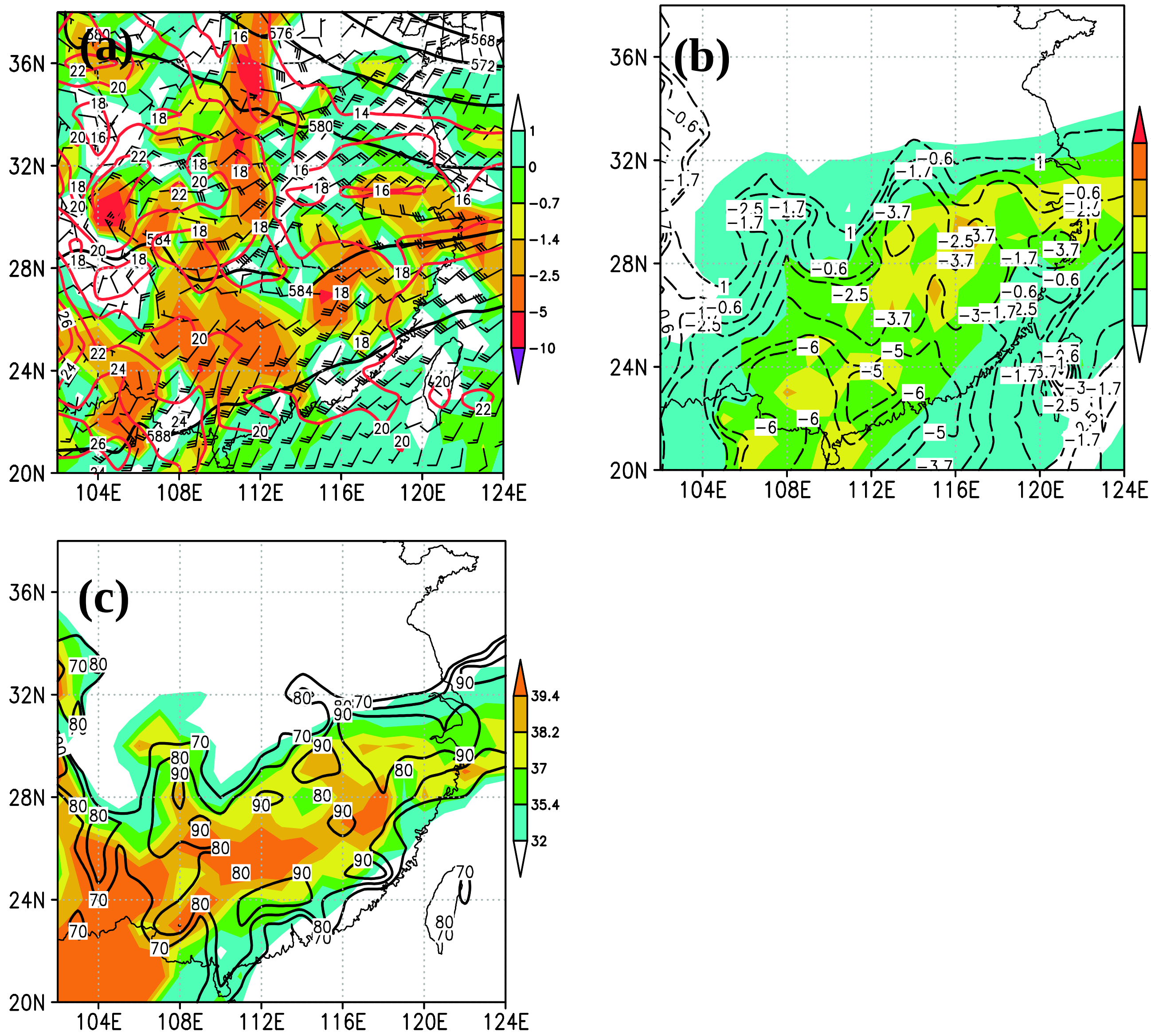

Figure 9. The 48-h synoptic pattern and parameter distribution valid at 20:00 BT on 15 May 2015 provided 48 h in advance by the NCEP GFS dataset; (**a**) 925 hPa divergence (10^{-5} s^{-1}, negative shading with legend at right), 850 hPa wind field (where a half-bar represents 2 m s^{-1}, a full bar represents 4 m s^{-1}, and a flag represents 20 m s^{-1}), temperature (red line, °C), and 500 hPa isobars (solid black line). (**b**) The PWAT (shaded with legend at right) and BLI (dashed black lines, °C). (**c**) The KI (shaded with legend at right) with the 850 hPa relative humidity greater than 70% (black solid line, %).

With these predicted environmental conditions, a large area is predicted to be at a high probability of SDHR. Much SDHR is reported by AWS located in the areas with a certain probability, but there are false alarms. The maximum CSI_{ave} weight group has higher probabilities at a great area compared with the maximum CSI weight group (Figure 10). The averaged SDHR probability of 84 groups shows many similar results. The standard deviation (Figure 10d) is much smaller over the predicted field, indicating a relatively small variance. The misses and false alarms of SDHR, in this case, indicate there is still some room for improvement.

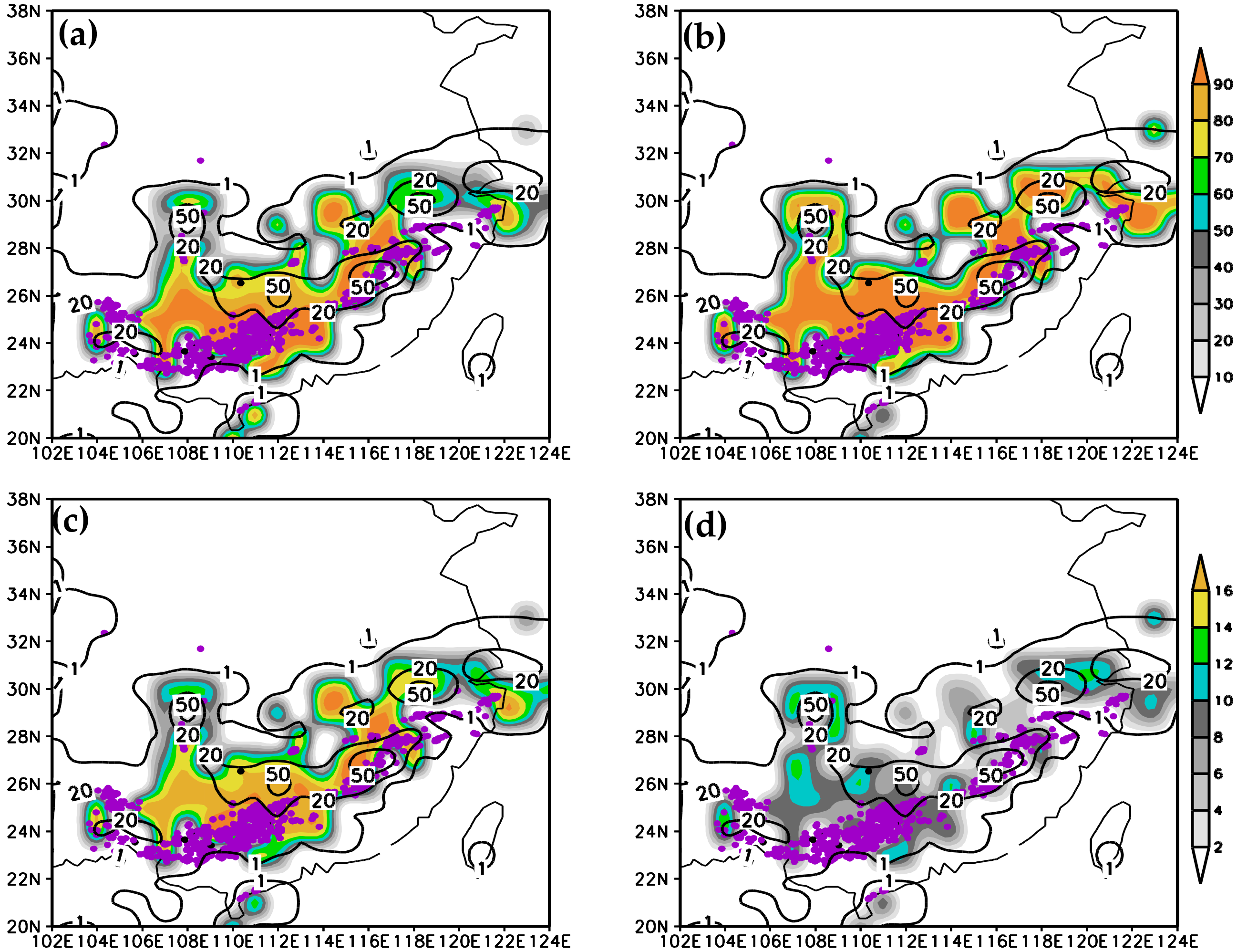

Figure 10. Comparison of predicted 48-h SDHR probability (shaded) valid at 20:00 BT; (**a**) is for the maximum CSI group with weights of No. 1 in Table 4, (**b**) is for the maximum CSI_{ave} group with weights of No. 6 in Table 4, (**c**) is the average of the 84 groups, and (**d**) is the corresponding standard deviation of (**c**). The available SDHR observations reported by AWS from 17:00 to 23:00 BT on 15 May 2015 are shown as purple dots. The solid lines in each panel are the NCEP-GFS-predicted six-hour rainfall accumulation (mm) from 17:00 to 23:00 BT on 15 May 2015.

5. Conclusions and Discussion

SDHR can be predicted from environmental conditions. However, the relative importance of instability, moisture content, and dynamic lifting varies between events. We introduce here an objective forecasting method for SDHR, taking the ingredients-based methodology. The approach is based on the common view that the moisture content, the instability, and the dynamical forcing are necessary ingredients for SDHR. The parameters indicating different aspects of the environmental conditions are chosen as predictors by comparing the discrimination of SDHR from both no rainfall and ordinary rainfall from the candidate parameters. A fuzzy logic approach using the selected predictors is adopted, and the probability of SDHR with various weight settings is evaluated. The objective SDHR products show strong positive skills within 60 h compared with the reference. Although weights for the SDHR with the highest maximum CSI and highest CSI_{ave} are much different, the case studies show similar patterns for the SDHR probabilities, indicating that the pattern of the SDHR probability is mainly determined by the environmental conditions rather than the weights.

The significant improvement compared to the reference could be determined by the intrinsic property that the various combinations favorable for SDHR could be covered. Luo et al. [3] summarized four main synoptic patterns leading to extreme hourly rainfall over China. The four synoptic patterns are far from enough to cover all the possible combinations. There might be no two synoptic patterns that are the same. The relative importance of the moisture content, instability, and dynamical lifting in a specific case can be seen. The obtaining of SDHR probability with the piecewise linearization of predictors reveals that the ingredients of moisture, instability, and lifting are complementary. The weakness of one ingredient could be made up for by the strengthening of the other one or two ingredients. The studied two case examples provide notable proof of this. Of the studied two cases, the notable environmental features for typhoon Soudelor would be the strong low-level convergence and the huge amount of water vapor content. For the ingredient-based methodology, the lack of enough instability does not favor heavy rainfall. The objective forecasting results show even weak to moderate instability is enough for a high probability of SDHR. Compared to the typhoon case, the second has strong lifting conditions and strong instability, but only moderate moisture content. It is one of the most challenging conditions the forecaster faced in spring. We can see the SDHR probability is still high. However, there is an overestimate. The forecasters can be remaindered in the short term. It is unimaginable for the manually produced SDHR forecasts to have similar coverage. The objective forecasting method provides evidence for the ingredients-based methodology that "sufficiency" is relative [45]. The insufficiency of a specific ingredient could still be strong enough to produce SDHR when coupled with the other ingredients with appropriate strength.

The representativeness of selected predictors is also important. Of the predictors used in this study, the BLI only represents the latent instability. KI is also used as an indicator of latent instability, although it has a two-way meaning. For the dynamic conditions, only the large-scale DIV_{925} is currently recognized as dynamical forcing. Local terrain effects [46] playing important roles in local SDHR are not taken into consideration. Even the local small-scale terrain can slow down the movement of surface weak convergence lines and enhance the temperature difference, and finally forms the local environment conditions favoring SDHR [8]. Application to high-resolution models could improve the influence of local terrain effects. Due to this incomplete coverage of the atmospheric environmental conditions, some of the SDHR could not be well predicted. More work should be carried out to improve the objective method and give it more wide applicability.

Author Contributions: Conceptualization, F.T., X.Z. and K.X.; methodology, F.T. and X.Z.; software, F.T.; validation, F.T. and J.S.; formal analysis, F.T.; investigation, F.T.; resources, X.Z.; data curation, F.T.; writing—original draft preparation, F.T. and Y.Z.; writing—review and editing, J.S. and K.X.; visualization, F.T.; supervision, K.X.; project administration, X.Z.; funding acquisition, X.Z. All authors have read and agreed to the published version of the manuscript.

Funding: This work was supported jointly by the National Key R&D Program of China (Grants 2017YFC1502003), the National Science Foundation of China (Grants U2142202), and the National Science Foundation for Young Scientists of China (Grants 41505080).

Institutional Review Board Statement: Not applicable.

Informed Consent Statement: Not applicable.

Data Availability Statement: The hourly rainfall observations are available at https://data.cma.cn/data/cdcindex/cid/f0fb4b55508804ca.html (accessed on 22 April 2022), and the NCEP GFS data are available at https://rda.ucar.edu/datasets/ (accessed on 22 April 2022).

Acknowledgments: We are grateful to the editors and the anonymous reviewers for their valuable comments. The help from Lulin Xue (NCAR) is also appreciated and acknowledged.

Conflicts of Interest: The authors declare no conflict of interest.

References

1. Brooks, H.E.; Stensrud, D.J. Climatology of heavy rain events in the United States from hourly precipitation observations. *Mon. Weather Rev.* **2000**, *128*, 1194–1201. [CrossRef]
2. Hitchens, N.M.; Brooks, H.E.; Sshumachs, R.S. Spatial and temporal characteristics of heavy hourly rainfall in the United States. *Mon. Weather Rev.* **2013**, *141*, 4564–4575. [CrossRef]
3. Luo, Y.L.; Wu, M.W.; Ren, F.M.; Li, J.; Wong, W.-K. Synoptic situations of extreme hourly precipitation over China. *J. Clim.* **2016**, *29*, 8703–8719. [CrossRef]
4. Zheng, Y.G.; Gong, Y.D.; Chen, J.; Tian, F.Y. Warm-season diurnal variations of total, stratiform, convective, and extreme hourly precipitation over Central and Eastern China. *Adv. Atmos. Sci.* **2019**, *36*, 143–159. [CrossRef]
5. Medlin, J.M.; Kimball, S.K.; Blackwell, K.G. Radar and rain gauge analysis of the extreme rainfall during Hurricane Danny's (1997) landfall. *Mon. Weather Rev.* **2007**, *135*, 1869–1888. [CrossRef]
6. Liao, Y.S.; Li, J.; Wang, X.F.; Cui, C.G.; Li, W.J. A meso-β scale analysis of the torrential rain event in Jinan in 18 July 2007. *Acta Meteorol. Sin.* **2010**, *68*, 944–956. (In Chinese)
7. Yu, X.D. Investigation of Beijing extreme flooding on 21 July 2012. *Meteorol. Mon.* **2012**, *38*, 1313–1329. (In Chinese)
8. Tian, F.Y.; Zheng, Y.G.; Zhang, X.L.; Zhang, T.; Lin, Y.J.; Zhang, X.W.; Zhu, W.J. Structure, triggering, and maintenance mechanism of convective systems during the Guangzhou extreme rainfall on 7 May 2017. *Meteorol. Mon.* **2018**, *44*, 469–484. (In Chinese)
9. Yin, J.F.; Gu, H.D.; Liang, X.D.; Yu, M.; Sun, J.S.; Xie, Y.X.; Li, F.; Wu, C. A possible dynamic mechanism for rapid production of the extreme hourly rainfall in Zhengzhou City on 20 July 2021. *J. Meteorol. Res.* **2022**, *36*, 6–25. [CrossRef]
10. Davis, R.S. Flash flood forecast and detection methods. In *Severe Convective Storms*; Doswell, C.A., III, Ed.; American Meteorological Society: Boston, MA, USA, 2001; pp. 481–525.
11. Cao, Y.H.; Wu, Z.L.; Xu, Z.Y. Effects of rainfall on aircraft aerodynamics. *Prog. Aerosp. Sci.* **2014**, *71*, 85–127. [CrossRef]
12. Yan, H.F.; Gallus, W.A., Jr. An evaluation of QPF from the WRF, NAM, and GFS Models using multiple verification methods over a small domain. *Weather Forecast.* **2016**, *31*, 1363–1379. [CrossRef]
13. Huang, L.; Luo, Y.L. Evaluation of quantitative precipitation forecasts by TIGGE ensemble for south China during the presummer rainy season. *J. Geophys. Res. Atmos.* **2017**, *122*, 8494–8516. [CrossRef]
14. Doswell, C.A., III; Brooks, H.E.; Maddox, R.A. Flash flood forecasting: An ingredients-based methodology. *Weather Forecast.* **1996**, *11*, 560–580. [CrossRef]
15. Fankhauser, J.C. Estimates of thunderstorm precipitation efficiency from field measurements in CCOPE. *Mon. Weather Rev.* **1988**, *116*, 663–684. [CrossRef]
16. May, P.T.; Rajopadhyaya, D.K. Vertical velocity characteristics of deep convection over Darwin, Australia. *Mon. Weather Rev.* **1999**, *127*, 1056–1071. [CrossRef]
17. Lepore, C.; Allen, J.T.; Tippett, M.K. Relationships between hourly rainfall intensity and atmospheric variables over the Contiguous United States. *J. Clim.* **2016**, *29*, 3181–3197. [CrossRef]
18. Lenderink, G.; Barbero, R.; Loriaux, J.M.; Fowler, H.J. Super-clausius-clapeyron scaling of extreme hourly convective precipitation and its relation to large-scale atmospheric conditions. *J. Clim.* **2017**, *30*, 6037–6052. [CrossRef]
19. Nielsen, E.R.; Schumacher, R.S. Dynamical insights into extreme short-term precipitation associated with supercells and mesovortices. *J. Atmos. Sci.* **2018**, *75*, 2983–3009. [CrossRef]
20. Doswell, C.A., III. The distinction between large-scale and mesoscale contribution to severe convection: A case study example. *Weather Forecast.* **1987**, *2*, 3–16. [CrossRef]
21. Tang, W.Y.; Zhou, Q.L.; Liu, X.H.; Zhu, W.J.; Mao, X. Analysis on verification of national severe convective weather categorical forecasts. *Meteorol. Mon.* **2017**, *43*, 67–76. (In Chinese)
22. Tian, F.Y.; Zheng, Y.G.; Zhang, T.; Mao, D.Y.; Tang, W.Y.; Zhou, Q.L.; Sun, J.H.; Zhao, S.X. Sensitivity analysis of short-duration heavy rainfall related diagnostic parameters with point-area verification. *J. Appl. Meteorol. Sci.* **2015**, *26*, 385–396. (In Chinese)
23. Tian, F.Y.; Zheng, Y.G.; Zhang, T.; Zhang, X.L.; Mao, D.Y.; Sun, J.H.; Zhao, S.X. Statistical characteristics of environmental parameters for warm season short-duration heavy rainfall over Central and Eastern China. *J. Meteorol. Res.* **2015**, *29*, 370–384. [CrossRef]
24. Li, Y.D.; Gao, S.T.; Liu, J.W. A calculation of convective energy and the method of severe weather forecasting. *J. Appl. Meteorol. Sci.* **2004**, *15*, 10–20. (In Chinese)
25. Schmeit, M.J.; Kok, K.J.; Vogelezang, D.H.P. Probabilistic forecasting of (severe) thunderstorms in the Netherlands using model output statistics. *Weather Forecast.* **2005**, *20*, 134–148. [CrossRef]
26. Pang, G.Q.; He, J.; Huang, Y.M.; Zhang, L.H. A binary logistic regression model for severe convective weather with numerical model data. *Adv. Meteorol.* **2019**, *2019*, 6127281. [CrossRef]
27. Hill, A.J.; Herman, G.R.; Schumacher, R.S. Forecasting severe weather with random forests. *Mon. Weather Rev.* **2020**, *148*, 2135–2161. [CrossRef]
28. Kistler, R.; Kalnay, E.; Collins, W.; Saha, S.; White, G.; Woollen, J.; Chelliah, M.; Ebisuzaki, W.; Kanamitsu, M.; Kousky, V.; et al. The NCEP-NCAR 50-Year Reanalysis: Monthly means CD-ROM and documentation. *Bull. Am. Meteorol. Soc.* **2001**, *82*, 247–268. [CrossRef]
29. Chen, C.S.; Lin, Y.-L.; Zeng, H.-T.; Chen, C.-Y.; Liu, C.-L. Orographic effects on heavy rainfall events over northeastern Taiwan during the northeasterly monsoon season. *Atmos. Res.* **2013**, *122*, 310–335. [CrossRef]

30. Tao, S.Y. *Torrential Rain of China*; Science Press: Beijing, China, 1980; pp. 1–225. (In Chinese)
31. Trenberth, K.E. Atmospheric moisture recycling: Role of advection and local evaporation. *J. Clim.* **1999**, *12*, 1368–1381. [CrossRef]
32. Galway, J.G. The lifted index as a predictor of latent instability. *Bull. Am. Meteorol. Soc.* **1956**, *37*, 528–529. [CrossRef]
33. Zimmermann, H.J. *Fuzzy Set Theory and Its Applications*, 4th ed.; Springer Science & Business Media, LLC: Berlin, Germany, 2001; pp. 141–160.
34. Mueller, C.; Saxen, T.; Roberts, R.; Wilson, J.; Betancourt, T.; Dettling, S.; Oien, N.; Yee, J. NCAR Auto-nowcast system. *Weather Forecast.* **2003**, *18*, 545–561. [CrossRef]
35. Berenguer, M.; Sempere-Torres, D.; Corral, C.; Sanchez-Diezma, R. A fuzzy logic technique for identifying nonprecipitation echoes in radar scans. *J. Atmos. Ocean. Technol.* **2006**, *23*, 1157–1180. [CrossRef]
36. Kuk, B.J.; Kim, H.I.; Ha, J.S.; Lee, H.K. A fuzzy logic method for lightning prediction using thermodynamic and kinematic parameters from radio sounding observations in South Korea. *Weather Forecast.* **2012**, *27*, 205–217. [CrossRef]
37. Lin, P.-F.; Chang, P.-L.; Jou, B.J.-D.; Wilson, J.W.; Roberts, R.D. Objective prediction of warm season afternoon thunderstorms in northern Taiwan using a fuzzy logic approach. *Weather Forecast.* **2012**, *26*, 44–60. [CrossRef]
38. Schroeer, K.; Kirchengast, G.; Sungmin, O. Strong dependence of extreme convective precipitation on gauge network density. *Geophys. Res. Lett.* **2018**, *45*, 8253–8263. [CrossRef]
39. Chen, J.; Zheng, Y.G.; Zhang, X.L.; Zhu, P.J. Distribution and diurnal variation of warm-season short-duration heavy rainfall in relation to the MCSs in China. *J. Meteorol. Res.* **2013**, *27*, 868–888. [CrossRef]
40. Li, W.H.; Yu, R.C.; Zhang, M.H.; Lin, W.Y.; Chen, H.M.; Li, J. Regimes of diurnal variation of summer rainfall over subtropical east Asia. *J. Clim.* **2012**, *25*, 3307–3320.
41. Dai, Z.J.; Yu, R.C.; Li, J.; Chen, H.M. The characteristics of summer precipitation diurnal variation in three reanalysis datasets over China. *Meteorol. Mon.* **2011**, *37*, 21–30. (In Chinese)
42. Zhou, C.L.; Wang, K.C. Contrasting daytime and nighttime precipitation variability between observations and eight reanalysis products from 1979 to 2014 in China. *J. Clim.* **2017**, *30*, 6443–6464. [CrossRef]
43. Ren, F.M.; Yang, H. An overview of advances in typhoon rainfall and its forecasting researches in China during the past 70 years and future prospects. *Torrent. Rain Disast.* **2019**, *38*, 526–540. (In Chinese)
44. Xu, W.X.; Zipser, E.J. Properties of deep convection in tropical continental, monsoon, and oceanic rainfall regimes. *Geophys. Res. Lett.* **2012**, *39*. [CrossRef]
45. Schultz, D.M.; Cortinas, J.V.; Doswell, C.A., Jr. Comments on "An operational ingredients-based methodology for forecasting midlatitude winter season precipitation". *Weather Forecast.* **2002**, *17*, 160–167. [CrossRef]
46. Xu, W.X.; Zisper, E.J.; Chen, Y.-L.; Liu, C.; Liou, Y.-C.; Lee, W.-C.; Jou, B.J.-D. An orography-associated extreme rainfall event during TiMREX: Initiation, storm evolution, and maintenance. *Mon. Weather Rev.* **2012**, *140*, 2555–2574. [CrossRef]